RSC Advances

PAPER

View Article Online
View Journal | View Issue

Cite this: *RSC Adv.*, 2015, **5**, 10018

Ultrasound-modulated microstructure of PbS film in ammonia-free chemical bath deposition

Libo Fan,[abc] Peng Wang,[a] Qiuquan Guo,[c] Hongpei Han,[a] Ming Li,[a] Zifa Chen,[a] Haifeng Zhao,[d] Dongxing Zhang,[c] Zhi Zheng*[b] and Jun Yang*[c]

Received 5th November 2014
Accepted 22nd December 2014

DOI: 10.1039/c4ra13921f

www.rsc.org/advances

In this work, ultrasound was used as an efficient way to solve the non-uniform nucleation over large-scale substrate and to modulate film microstructure for performance improvement. Lead sulfide (PbS), as one of the most important IV–VI group semiconductors, was employed to prepare large-scale uniform films with the assistance of ultrasound in ammonia-free chemical bath deposition (CBD). The characteristics of PbS films, including crystalline structure, stoichiometry, surface morphology, cross-section structure, thickness, roughness and optical property were studied to reveal the modulating effect of ultrasound. In addition, the growth mechanism of PbS films was discussed. More importantly, PbS films prepared by ultrasound-assisted ammonia-free CBD provided better photoelectrochemical (PEC) performance with intense photosensitivity.

1 Introduction

It is of great interest to fabricate semiconductor films with large scale for the application in a variety of devices. Among numerous techniques, chemical bath deposition (CBD) is proved to be a convenient, low-temperature, low-cost, highly efficient and versatile process to fabricate various semiconductor films in large dimension on all types of hydrophilic substrates.[1–4] Recently, the newly developed ammonia-free CBD technique is verified to be a more environmentally friendly process and has better stability and reproducibility than the conventional, highly volatile and harmful CBD methods using ammonia.[5,6] However, the challenge of CBD is the uniform nucleation over large-scale substrate, which is possibly due to the weak turbulence around the edge of the substrate, resulting in non-uniform nucleation.[7,8] In order to obtain homogenous film, extra solution was often added to minimize the negative effect of the substrate, but it will increase chemical waste correspondingly.[7] Hence, in this study, ultrasound is proposed to be integrated into ammonia-free CBD to investigate its modulating effect on film uniformity and microstructure.

Ultrasound was introduced into chemistry—sonochemistry and has been widely investigated in recent years. The primary effect of ultrasound on continuum fluid is to impose an oscillatory pressure within an entire solution, which will produce unique hot spots with temperature exceeding 5000 K and pressure above 1000 atm, as well as heating or cooling rate over 10^{10} K s^{-1}.[9–11] These extreme transient conditions distinguish sonochemistry from other conventional synthetic techniques, such as photochemistry, electrochemistry, chemical vapor deposition and CBD. As a green and feasible method, it has a great advantage to optimize the chemical usage and reduce waste production fundamentally. Introducing ultrasound into CBD will not only ensure uniform nucleation over the entire substrate no matter how large it is, but also lead to the improvement of film microstructure, which has a tight relationship with film property.[7,12,13] Besides, CBD is the most convenient and frequently used technique to grow PbS film, which has been widely applied in infrared detectors, solar cells, photography and so on.[5,14,15] In this paper, lead sulfide (PbS) prepared by ammonia-free CBD is chosen to investigate the modulating effect of ultrasound on film uniformity and microstructure associated with crystalline structure, stoichiometry, growth mechanism, optical absorption, and photoelectrochemical (PEC) performance.

2 Experimental section

2.1 Materials

All reagents, lead acetate ($Pb(CH_3COO)_2 \cdot 3H_2O$), sodium hydroxide (NaOH), thiourea ($(NH_2)_2CS$), triethanolamine (TEA, $N(CH_2CH_2OH)_3$), ammonia ($NH_3 \cdot H_2O$), hydrogen peroxide (H_2O_2) and sodium sulfate (Na_2SO_4), were of analytical grade. Indium-Tin-Oxide-coated glass (ITO/glass), with a sheet resistance of 15 Ω sq^{-1}, was cut into 10 × 20 mm^2 or 30 × 40 mm^2 and used as substrate.

[a]School of Electrical Engineering, Xuchang University, Henan 461000, China
[b]Key Laboratory of Micro-Nano Materials for Energy Storage and Conversion of Henan Province, Institute of Surface Micro and Nano Materials, Xuchang University, Henan 461000, China. E-mail: zzheng@xcu.edu.cn
[c]Department of Mechanical & Materials Engineering, Western University, London, Ontario N6A 5B9, Canada. E-mail: jyang@eng.uwo.ca
[d]State Key Laboratory of Luminescence and Applications, Changchun Institute of Optics, Fine Mechanics and Physics, Chinese Academy of Sciences, Jilin 130033, China

2.2 Cleaning of ITO/glass

Substrate cleaning is very important to ensure the deposited film exhibits high quality and good adhesion. In this work, a series of solution-based steps were used. First, the substrates were immersed into an aqueous detergent and ultrasonically washed for 30 min to remove the grease and dust, followed by ultrasonically rinsing with deionized (DI) water for 10 min three times. Subsequently, they were boiled in a mixed solution of $NH_3 \cdot H_2O$, H_2O_2 and DI water with a volume ratio of 1 : 2 : 5 at 80 °C until no bubbles were generated to remove any organic residue from the surface. Finally, they were ultrasonically rinsed again with DI water for 10 min three times, and dried in a vacuum oven at 80 °C for 2 h.

2.3 CBD of PbS films

The PbS film was deposited in a reactive solution prepared by sequentially adding aqueous solutions of 2.5 mL 0.5 M $Pb(CH_3COO)_2 \cdot 3H_2O$, 2.5 mL 2 M NaOH, 3 mL 1 M $(NH_2)_2CS$ and 2 mL 1 M $N(CH_2CH_2OH)_3$. The total volume was adjusted to 50 mL with DI water. The top area of ITO film was covered by tape for protection (yellow area in Fig. 1a and b), leaving ITO as an electrode to be connected with the external circuit. The back side was all covered to avoid film being deposited on the glass surface. In order to prevent the tape from falling off, blank glass slides were placed on the tapes on both sides and clamped by a clip. The prepared substrate was vertically immersed and fixed in the middle of beaker (Fig. 1a). Sample A was kept in a 70 °C bath for 1 h without ultrasound, while sample B was placed into an ultrasound bath with a frequency of 40 kHz and a power of 100 W for film deposition. Finally, the deposited PbS films were rinsed with DI water thoroughly to remove the unreacted or any other chemicals absorbed on the film surface and dried in a vacuum oven at 80 °C for 2 h.

2.4 Characterization

The X-ray diffraction (XRD) patterns were recorded on a Bruker D8 Advance diffractometer (nickel-filtered Cu Kα radiation, λ = 1.54178 Å, 40 kV, 40 mA) over the 2θ range of 20–60° with a step size of 0.02°. Field-emission scanning electron microscopy (FE-SEM, S-4800, HITACHI) was used to get high-resolution images of the surface. In order to confirm the chemical composition and stoichiometry of PbS films, both energy-dispersive X-ray spectroscopy (EDX, genesis 2000, EDAX) and X-ray photoelectron spectroscopy (XPS) were performed. The XPS was detected on a Kratos Axis Ultra spectrometer with monochromatic Al Kα radiation (1486.6 eV) as the exciting source. The survey spectrum was scanned within an area of 300 × 700 μm^2, and the binding energy was calibrated by referencing the C 1s peak at 284.6 eV. An atomic force microscope (AFM, Dimension 3100, Veeco) was used to investigate surface roughness. The standard cantilever with nominal spring constant of ~40 N m^{-1} was used, and tapping mode was applied to avoid surface damage. Optical absorption spectra were obtained on a UV-Vis-NIR spectrophotometer (Cary 5000, Varian) ranging from 0.5 eV to 3.5 eV at room temperature.

2.5 PEC measurement

PEC analysis was performed using a potentiostatic and three-electrode quartz cell. PbS film coated ITO/glass (~10 × 20 mm^2) was used as the working electrode (~10 × 10 mm^2 active area), while Pt wire acted as the counter electrode and a saturated calomel electrode (SCE) as reference (Fig. 1b). The working electrode was placed in the electrolyte of aqueous Na_2SO_4 (0.10 M) without any sacrificial reagent, and the conductive side was oriented facing the incident light named as front illumination. The light source was an ultraviolet (UV) lamp with a power of 6 W, the output of which was chopped by an automatic mechanical shutter with an interval of 1 s. The change of transient photocurrent density with time was recorded by an electrochemical workstation (CHI660D, CH Instrument Company, China). To eliminate the noise effect, the UV lamp was switched on once the background signal got stable, which usually takes ~5 s.

3 Results and discussions

3.1 Purity, crystal structure and crystallinity

As shown in the XRD patterns (Fig. 2), the ultrasound-assisted method is able to keep PbS film with high purity, cubic structure and good crystallinity. The two samples have similar patterns with no significant difference. Both diffraction peaks from PbS and ITO can be found in sample A (Fig. 2a) and B (Fig. 2b) by comparing standard PDF card no. 5-592 and the pattern of blank ITO/glass (Fig. 2c). The diffraction peaks of both components overlap at 30.1°. Both PbS films are

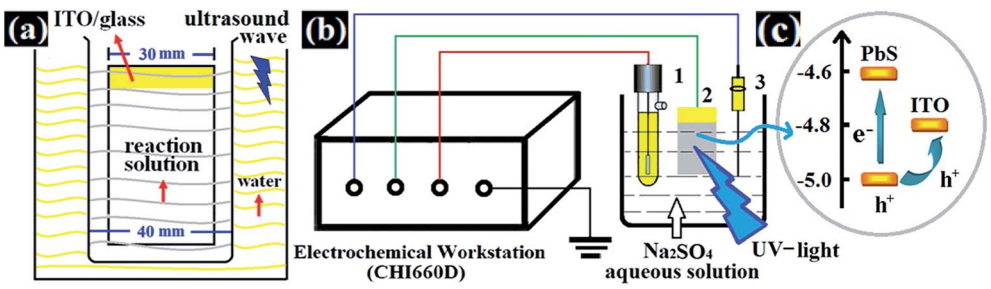

Fig. 1 Schematic illustration of (a) ultrasound-assisted CBD system, (b) PEC system: 1-SCE, 2-PbS/ITO/glass electrode and 3-Pt electrode, and (c) instantaneous photo-induced transition of holes.

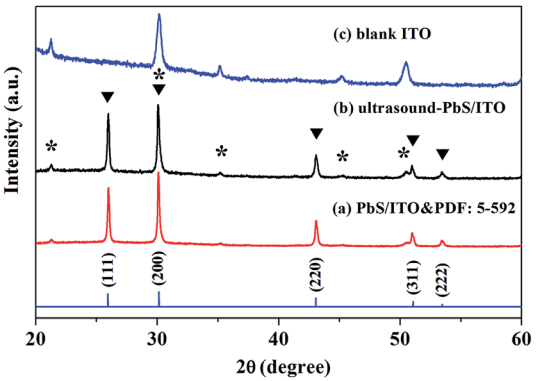

Fig. 2 XRD patterns of (a) sample A and standard PDF card no. 5-592, (b) sample B, and (c) blank ITO/glass. Diffraction peaks from ITO (*) and PbS (▼) are labeled.

polycrystalline essentially with a pure cubic structure. Moreover, the lattice constants were calculated based on (111) peak, which have little deviation from standard bulk PbS ($a = 5.9362$ Å). No other peaks were detected except the ones for PbS and ITO, which further confirms the purity of PbS films. In addition, strong and sharp diffraction peaks demonstrate both PbS films, with or without the assistance of ultrasound, have good crystallinity.

3.2 Uniformity, surface morphology, thickness and cross-section structure

Ultrasound-assisted CBD can realize large-area deposition with great film uniformity. The film fabricated by conventional ammonia-free CBD presents gray and frosted-like surface (sample A, inset in Fig. 3a). Besides, film uniformity decreases significantly with the increase in deposition area. In order to solve the problem, ultrasound was introduced into the process of ammonia-free CBD. The obtained film showed dark-gray and mirror-like surface and good adhesion on the substrate according to tape testing (sample B, inset in Fig. 3b). Furthermore, the film has a great uniformity over the entire substrate even at the boundary, with a large size as much as 30 × 40 mm^2.

Ultrasound promotes the formation of a dense and smooth surface. The surface morphology and film thickness were further characterized by FE-SEM. Fig. 3a (sample A) and 3b (sample B) show that the surfaces of both samples are quite uniform with very few overgrown grains. By further magnifying, it can be seen that the surface of sample A (Fig. 3c) is composed of pebble-like grains with a diameter of ~500 nm and very well defined boundaries. In addition, gap exists distinguishably between different grains. Sample B (Fig. 3d), however, exhibits a compact surface with homogenous granular structure and sharp and well defined grain boundaries. The angular stone-like grains, ~300 nm dimension, match together well with each other without obvious gap. Moreover, ultrasound can suppress the growth of protrusions on the grain surface to generate a denser and smoother surface. For sample A, particle-like protrusions, with different sizes, grow on the grain surface. As labeled by red circles, ~10 nm protrusions can be seen, and they

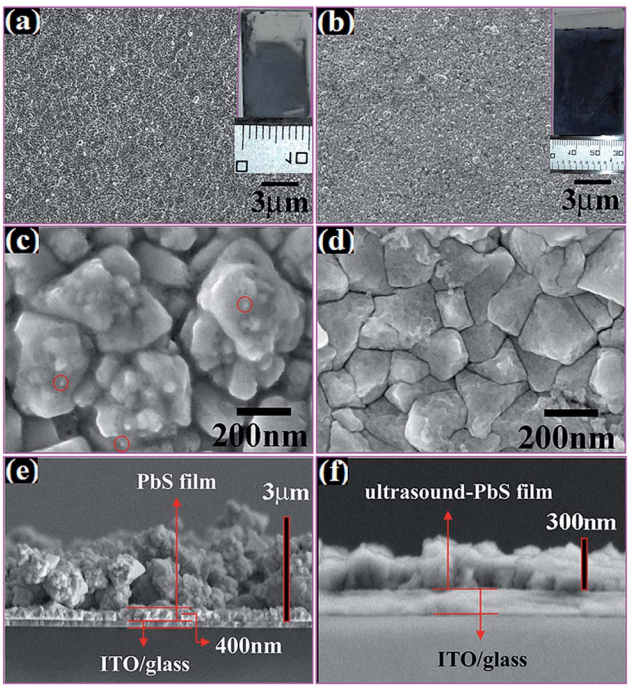

Fig. 3 FE-SEM images of (a), (c) and (e) for sample A, and (b), (d) and (f) for sample B at different magnifications; ~10 nm protrusions are labeled in circles in (c) partially. (e) and (f) are cross-section views. Inset of (a): optical image of sample A (10 × 20 mm^2); inset of (b): optical image of sample B (30 × 40 mm^2).

cause a blue-shifted interband absorption within PbS (Fig. 8b). As for sample B, the grain surface is relatively smooth without protrusions, which agrees well with reported results.[16,17]

Ultrasound can control the layer-like structure of film and slow down deposition rate to form a denser surface and thinner film. From the cross-section view (sample A in Fig. 3e and sample B in Fig. 3f), the two layers at the very bottom were identified as ITO and glass separately. Ultrasound-assisted PbS film (sample B) shows only one dense layer of ~300 nm rooted on the ITO/glass; however, the PbS film of sample A exhibits a two-layer structure as thick as ~3 μm, including a dense bottom layer with a thickness of ~400 nm and a loose top layer. The loose layer is deposited with ~1 μm grains, which were not found in sample B. These are consistent with previous results in literature.[7,17] Note that the grain dimension (~1 μm from side view) here for sample A is twice as large as the estimation from its top view (~500 nm), which is reasonable because the top view shows the surface part only but not the entire grain body in the film. Film thickness and cross-section structure modulated by ultrasound may originate from the optimization in growth mechanism, which will be discussed in the following part.

3.3 Chemical composition and stoichiometry

Both samples A and B have shown relatively balanced stoichiometry, with the atomic ratio of element Pb to S within PbS film being nearly equal to unity, whereas sample B was more near-stoichiometric than sample A, which verified that ultrasound

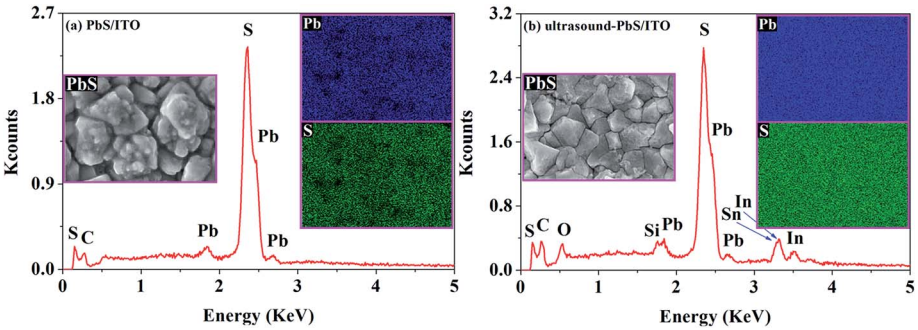

Fig. 4 EDX spectra of (a) sample A and (b) sample B. Inserts: elemental maps for Pb (upper right sides in a and b), S (lower right sides in a and b) and corresponding FE-SEM images of sample A (left side in a) and sample B (left side in b).

was able to promote the formation of PbS film with better stoichiometry.

The chemical composition of sample A (Fig. 4a) or B (Fig. 4b) was detected by EDX spectra. The peaks from Pb, S and carbon (C) were presented in both samples, while the peaks from O, In, Sn and silicon (Si) also appeared for sample B,[18] which were attributed to the substrate (ITO/glass) due to the thinner PbS film on it with respect to sample A. The presence of element C in both samples may be from adsorbed gaseous molecules for high surface-to-volume ratio of the PbS film with pebble-like (sample A) or angular stone-like (sample B) surface microstructure. No other peaks from impurities were observed, which demonstrated the purity of both samples. Quantitative analysis indicated that both films exhibited a slightly higher content of element Pb. The atomic ratio of element Pb to S was ~1.05 : 1 for sample A and 1.02 : 1 for sample B. The elemental maps illustrated that the distribution of element Pb and S on the film surface of the sample B (inserts in Fig. 4b) was more uniform than that of sample A (insets in Fig. 4a), which was most likely because the film surface of the sample B was smoother than that of sample A.

The stoichiometry of sample A (Fig. 5a) and B (Fig. 5b) was further confirmed by XPS survey spectrum. The presence of Pb, S, C and O without any other elements from impurities was observed, which suggested once again the purity of PbS films. All observed binding-energy values were indexed on the handbook of elements and native oxides (1999 XPS International, Inc.).[19] Peak-area quantification of Pb and S gave the atomic ratio of Pb to S as 1.07 : 1 for sample A, while it was reduced to 1.05 : 1 for sample B. Although the film surface of sample B was a little bit rich in element Pb, it was still near-stoichiometric within experimental uncertainty limits.

Overall, elemental content analysis indicates that the content of element Pb within sample B was reduced to approach closer to the stoichiometry of the PbS compound. As a consequence, some defects like S vacancies or Pb interstitial will be inhibited at a certain level, which will facilitate the application of PbS film in photovoltaic devices.

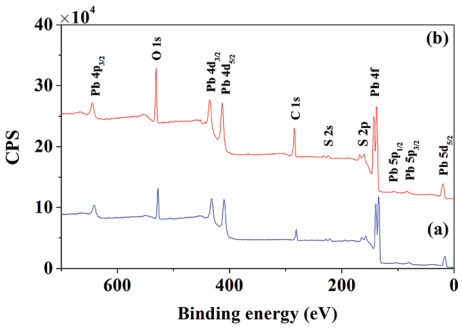

Fig. 5 XPS spectra of (a) sample A and (b) sample B.

3.4 Surface topography and roughness

Surface topography and roughness were investigated by AFM (Fig. 6), which also indicated that ultrasound promoted the formation of a smooth surface. The three-dimensional (3D) AFM image displays surface topography, a visualized surface roughness (sample A in Fig. 6a and sample B in Fig. 6b). The root-mean-square roughness (R_q) of sample A was 19.5 nm and the average roughness (R_a) was 16.1 nm, while the R_q of sample B was 13.5 nm and the R_a was 11.0 nm. All the above data are comparable to other reported roughness of PbS films prepared by CBD.[20,21]

3.5 Reaction and growth mechanisms

In general, the reaction mechanisms of both samples may be the same when the power of ultrasound is not high. During the reaction, TEA acts as a complexing agent to control the release rate of Pb ions [eqn (1) and (5)], and the alkaline hydrolysis of thiourea provides S^{2-} ions [eqn (2)–(4)]. As soon as the ionic-product constant (K_w) of Pb^{2+} and S^{2-} exceed the solubility-product constant of PbS ($K_{sp} = 1.1 \times 10^{-29}$),[22] PbS will precipitate [eqn (5)], followed by the film deposition on the substrate. The typical steps of reaction involved in the growth process can be written as follows:[23,24]

$$Pb(CH_3COO)_2 \cdot 2H_2O + TEA \rightarrow Pb(TEA)^{2+} + 2(CH_3COO^-) + 2H_2O \quad (1)$$

$$(NH_2)_2CS + OH^- \rightarrow SH^- + NCNH_2 + H_2O \quad (2)$$

$$NCNH_2 + H_2O \rightarrow NH_4CNO \quad (3)$$

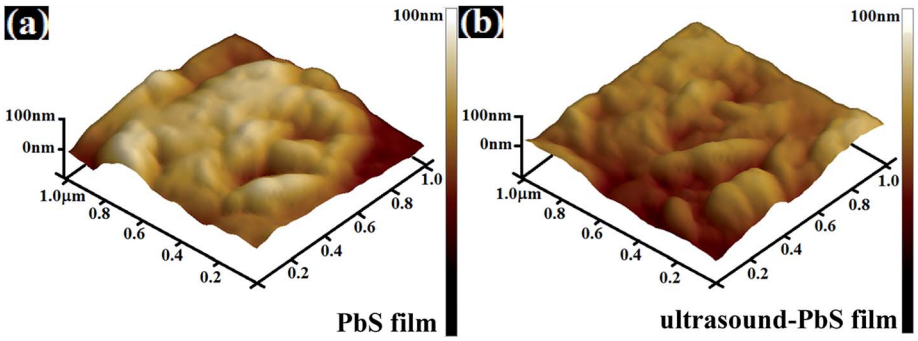

Fig. 6 3D AFM images of (a) sample A and (b) sample B.

$$OCN^- + 2H_2O \rightarrow HCO_3^- + NH_3 \quad (4)$$

$$Pb(TEA)^{2+} + SH^- + OH^- \rightarrow PbS\downarrow + H_2O + TEA \quad (5)$$

The schematic image of growth mechanisms for PbS films without (sample A) and with (sample B) ultrasound modulation is shown in Fig. 7. As reported, "ion-by-ion" and "cluster-by-cluster" are two main growth mechanisms in the conventional CBD process.[23,25] Similar conditions of solution permit the two mechanisms to take place individually, simultaneously or sequentially with "ion-by-ion" followed by "cluster-by-cluster."[26,27] Usually, ammonia-free CBD promotes the "ion-by-ion" growth at an earlier stage resulting in a compact and highly oriented film with a large refraction index (Fig. 7c). Immediately after that, a large amount of Pb^{2+} and S^{2-} produce a fast formation of PbS colloids leading to the "cluster-by-cluster" deposition[26,28] (Fig. 7a). In consequence, the deposited film consists of a dense inner "ion-by-ion" layer and a loose external "cluster-by-cluster" layer, which is reflected by sample A (Fig. 3e). However, with the modulation of ultrasound, the formation of clusters was inhibited (Fig. 7b), and thus there is only one dense "ion-by-ion" layer but no loose "cluster-by-cluster" layer in sample B (Fig. 3f).

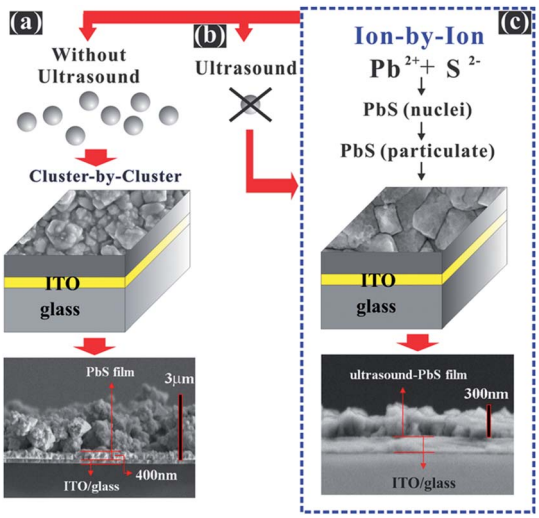

Fig. 7 Schematic image for growth mechanisms of CBD (a) without ultrasound for "ion-by-ion" followed by "cluster-by-cluster" depositions (sample A); (b) with ultrasound for breaking up the clusters, and (c) ion-by-ion deposition only (sample B).

Although the effect of ultrasound on chemical reactions is not well understood yet, it is mostly believed that an acoustic cavitation takes place in the solution,[9,10,29] which was thought to be the most important effect of ultrasound in both chemical and crystallizing systems.[7,13,30,31] Basically, applying ultrasound into a chemical bath will impose an oscillatory pressure on the solution. At a low intensity of ultrasound, this pressure will induce an acoustic streaming (motion and mixing within the solution), while at high intensity, local pressure will fall below the vapor pressure of solution and produce tiny bubbles or cavities. Further increasing the intensity will produce negative transient pressure within the solution, which will both enhance bubble growth and generate new cavities. Overall, the cavitation, including creation, growth and collapse of gas vacuoles in solution, can actively break up large clusters into smaller ones.[7,31,32] Therefore, it is reasonable to believe that applying ultrasound into ammonia-free CBD will suppress "cluster-by-cluster" deposition.[7] As an external source of energy, the other benefit of ultrasound is believed to provide highly intensive mixing or agitation, which can accelerate uniform nucleation over large-scale substrate and also suppress the growth of substructures on the film surface.[7,13,31,33] As a result, film microstructure is modulated, and the whole film properties are improved correspondingly.

3.6 Optical absorption

Energy-level structure was studied by optical absorption (Fig. 8). It can be seen that ultrasound was able to not only maintain the interband absorption of PbS but also provide much higher absorption intensity. Moreover, no blue-shifted interband absorption of PbS appearing in sample B indicates that ultrasound has successfully suppressed the generation of substructure, which further confirms the microstructure analysis above. To distinguish the influence of substrate, the absorption spectrum of ITO/glass was measured first (Fig. 8a). ITO/glass is an n-type semiconductor with a large band-gap of ~4 eV, which exhibits an edge below 1.3 eV from the free-carrier absorption of ITO.[34] That means infrared photons can excite electrons from near bottom to higher energy levels of the conduction band.

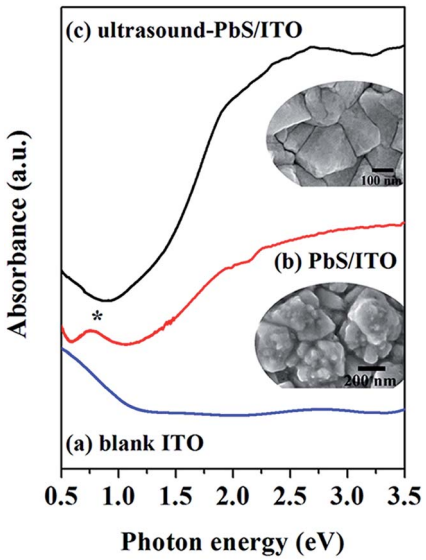

Fig. 8 Optical absorption spectra of (a) blank ITO/glass, (b) sample A, and (c) sample B. Inset: FE-SEM images of sample A (lower right) and B (upper right).

Most importantly, it is nearly transparent from 1.3 eV to 3.5 eV for ITO/glass.

As mentioned, sample A and B presented similar color, gray and dark gray respectively. Accordingly, they possessed the same trend of absorption spectra (Fig. 8b and c). The band between 1.3 eV and 3.5 eV may come primarily from the inter-band absorption of bulk PbS, which should start from the location of the optical band gap for bulk PbS at ~0.41 eV at room temperature. However, it overlapped with the free-carrier absorption of ITO. Interband absorption indicates UV photons can excite electrons from valence band to conduction band, and this result agrees well with our previous report about *in situ* growth of PbS film on Pb foil.[35] It is worthy to note that sample B presented a color darker than that of sample A. Correspondingly, the absolute absorption intensity of sample B was about twice as high as that of sample A. More importantly, the film with unique microstructure can trap more light to enhance broadband optical absorption.[36,37] Although the PbS film in sample B was ~10 times thinner than that of sample A, sample B can trap light more efficiently due to the improved microstructure by the introduction of ultrasound. The edge below 1.3 eV should be dominated by free carrier absorption of ITO; however, a different peak appears at ~0.75 eV in sample A, which is supposed to originate from a blue-shifted interband absorption within PbS for quantum confinement effect. Because PbS has a large exciton Bohr radius (18 nm) at room temperature, many protrusions growing on grain surfaces, especially with a ~10 nm diameter (Fig. 3c), exhibited the same absorption feature as PbS quantum dots of ~10 nm.[38,39]

3.7 Transient photocurrent response

Current PEC investigation demonstrates that ultrasound-assisted PbS film is able to suppress the phenomenon of current overshoot during on–off switching and produce a comparable photosensitivity with the ~10 times thicker traditional PbS film. Transient photocurrent response of the PEC system (Fig. 1b) was measured and the representative change of transient photocurrent density (J_p) with time was plotted under intermittent UV irradiation at 0 V bias *vs.* SCE (Fig. 9). Both samples exhibited photocurrents with great stability and reproducibility during successive on–off cycles of UV light. Photocurrent appeared upon UV irradiation, went down to maximum immediately, and disappeared instantly once the irradiation was switched off. This is the characteristic of cathodic photocurrent and suggests both PbS films (samples A and B) exhibit a p-type conductivity.[40,41] Based on PEC theories, charge carriers will be generated and separated at electrode/electrolyte interface and then transited between electrode surface and underlying substrate because of semiconductor photo-excitation.[42] Accordingly, the cathodic photocurrent is dominated by instantaneous photo-induced hole transition between electrolyte and ITO/glass *via* PbS film (Fig. 2c).[43]

Although sample A was ~10 times thicker than sample B, sample A (Fig. 9a) and B (Fig. 9b) showed roughly the same J_p of ~1.9 μA cm^{-2} and ~1.8 μA cm^{-2} respectively. In dark conditions, a current density (dark current J_d) of ~0.6 μA cm^{-2} was observed in both samples. The J_p to J_d ratio (*i.e.* photosensitivity[43,44]) was ~3.2 for sample A and ~3.0 for sample B, which indicated the ITO/glass can be sensitized efficiently by both samples. However, many other factors such as bias voltage, electrolyte solution and light source can affect the magnitude of photocurrent or dark current.[41,42] Among those factors, the microstructure of film surface has the most significant influence on the PEC performance.

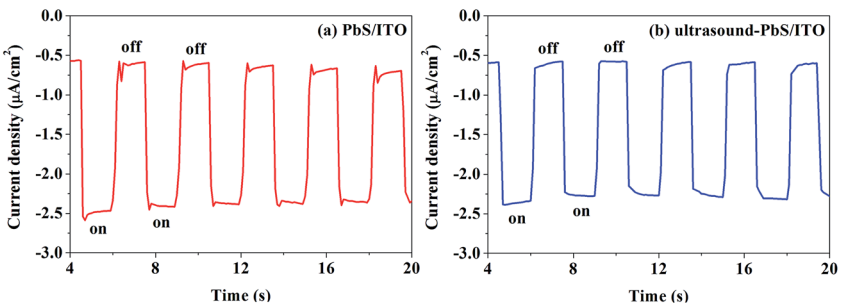

Fig. 9 Transient photocurrent response of (a) sample A and (b) sample B.

Fig. 9a shows that the overshot current of sample A at on–off switching did not occur in sample B. A similar phenomenon was also often observed in other inorganic semiconductor based PEC cells, such as NiO nanoparticles on fluorine doped tin oxide (FTO),[40] $Pb(Zr_xTi_{12x})O_3$ films on ITO/glass,[45] ZnO/tetrasulfophthalocyanine hybrid film,[46] and Cu_2S nanowire film on Cu electrode.[40] The overshoot of cathodic photocurrent at the very beginning of UV illumination demonstrates a significant accumulation of photo-generated electrons on the surface of the PbS/ITO electrode due to the existence of surface states.[46,47] Subsequently, the decay towards the steady state is developed from the recombination of these surface-trapped electrons with holes. Similarly, an anodic current appeared and then decreased gradually to a stable dark current just after the end of UV illumination, which is attributed to the continuing flux of holes into the surface of the PbS/ITO electrode and then recombining with electrons remaining in the surface states. As described in FE-SEM and AFM sections, the surface of sample A was rougher than that of sample B from its more complicated surface microstructure. It is reasonable to believe that rough surface will induce more surface states. Therefore, fewer surface states existed in sample B leading to no obvious overshoot of current.

4 Conclusions

In our ammonia-free CBD, the problem—decreasing of film uniformity with the increasing of deposited area—has been resolved efficiently by the introduction of ultrasound. Ultrasound was able to modulate film microstructure greatly and keep the film with high purity, cubic structure, good crystallinity, balanced stoichiometry, interband absorption, stable photosensitivity and p-type conduction. In addition, it can suppress "cluster-by-cluster" deposition and the growth of substructure on the grain surface. As for cross-section structure, a dense "ion-by-ion" layer covered by a loose "cluster-by-cluster" layer, composed of many big pebble-like grains with apparent gap, was deposited on substrate without ultrasound. Differently, only one dense "ion-by-ion" layer was grown with the assistance of ultrasound. Due to the disappearance of the loose layer, ultrasound-assisted ammonia-free CBD often has much lower thickness. In addition, protrusions with different sizes grow on grain surfaces, especially those ~10 nm ones that can cause a blue-shifted interband absorption within PbS. Ultrasound-assisted film, however, consisted of angular stone-like grains, which match together well with each other without either obvious gap or protrusions. Therefore, a more uniform and smoother film surface was generated to reduce surface states, which exhibited more intense interband absorption, better photocurrent response without overshoot of current during on–off switching of the UV light. It is believed that the developed technique can be leveraged with other film preparation processes to obtain more uniform microstructure and better performance.

Acknowledgements

This work was supported by the Program for Science and Technology Innovation Talents and Teams in Universities of Henan Province (Grant no. 2012HASTIT033 and 14IRTSTHN022), the Aid Project for the Leading Young Teachers in Henan Provincial Institutions of Higher Education of China (Grant no. 2011GGJS-180), the Science Research Project of Henan education department (Grant no. 13A140742, 14A140020, 13A140749 and 14B140011), Science and Technology Project of Xuchang City (Grant no. 5013 and 1404006), National Natural Science Foundation of China (Grant no. 11004168 and 61306012), Natural Science and Engineering Research Council of Canada (NSERC), and Canada Foundation for Innovation (CFI).

Notes and references

1 Y. Chen, X. Zhang, Q. Tao, H. Yang, S. Su and Y. Mu, *RSC Adv.*, 2015, **5**, 1835–1840.
2 S. Hoang, S. P. Berglund, R. R. Fullon, R. L. Minter and C. B. Mullins, *J. Mater. Chem. A*, 2013, **1**, 4307–4315.
3 G. Hodes, *Phys. Chem. Chem. Phys.*, 2007, **9**, 2181–2196.
4 P. Nair, M. Nair, V. Garcıa, O. Arenas, A. C. Peña, I. Ayala, O. Gomezdaza, A. Sanchez, J. Campos and H. Hu, *Sol. Energy Mater. Sol. Cells*, 1998, **52**, 313–344.
5 J. Hernández-Borja, Y. Vorobiev and R. Ramírez-Bon, *Sol. Energy Mater. Sol. Cells*, 2011, **95**, 1882–1888.
6 A. Goudarzi, G. M. Aval, R. Sahraei and H. Ahmadpoor, *Thin Solid Films*, 2008, **516**, 4953–4957.
7 M. Kim, S. Lee and S. Sohn, *Thin Solid Films*, 2011, **519**, 1787–1793.
8 Y.-J. Oh, S.-H. Chung and M.-S. Lee, *Mater. Trans.*, 2004, **45**, 3005–3010.
9 K. S. Suslick, *science*, 1990, **247**, 1439–1445.
10 K. S. Suslick and D. J. Flannigan, *Annu. Rev. Phys. Chem.*, 2008, **59**, 659–683.
11 H. Xu, B. W. Zeiger and K. S. Suslick, *Chem. Soc. Rev.*, 2013, **42**, 2555–2567.
12 J. Yang and A. V. Walker, *Langmuir*, 2014, **30**, 6954–6962.
13 J. Y. Choi, K.-J. Kim, J.-B. Yoo and D. Kim, *Sol. Energy*, 1998, **64**, 41–47.
14 S. A. McDonald, G. Konstantatos, S. Zhang, P. W. Cyr, E. J. Klem, L. Levina and E. H. Sargent, *Nat. Mater.*, 2005, **4**, 138–142.
15 P. Nair, O. Gomezdaza and M. Nair, *Adv. Mater. Opt. Electron.*, 1992, **1**, 139–145.
16 A. Ichiboshi, M. Hongo, T. Akamine, T. Dobashi and T. Nakada, *Sol. Energy Mater. Sol. Cells*, 2006, **90**, 3130–3135.
17 X. Gao, X. Li and W. Yu, *Thin Solid Films*, 2004, **468**, 43–47.
18 J. A. Bearden, *Rev. Mod. Phys.*, 1967, **39**, 78–124.
19 B. V. Crist, *Handbooks of Monochromatic XPS Spectra*, XPS International, Inc., 1999.
20 T. Tohidi, K. Jamshidi-Ghaleh, A. Namdar and R. Abdi-Ghaleh, *Mater. Sci. Semicond. Process.*, 2014, **25**, 197–206.
21 R. Das and R. Kumar, *Mater. Res. Bull.*, 2012, **47**, 239–246.

22 B. Altıokka, M. C. Baykul and M. R. Altıokka, *J. Cryst. Growth*, 2013, **384**, 50–54.
23 P. O'Brien and J. McAleese, *J. Mater. Chem.*, 1998, **8**, 2309–2314.
24 F. Göde, E. Güneri, F. Emen, V. Emir Kafadar and S. Ünlü, *J. Lumin.*, 2014, **147**, 41–48.
25 M. Froment and D. Lincot, *Electrochim. Acta*, 1995, **40**, 1293–1303.
26 M. Sandoval-Paz and R. Ramírez-Bon, *Thin Solid Films*, 2009, **517**, 6747–6752.
27 T. P. Niesen and M. R. De Guire, *J. Electroceram.*, 2001, **6**, 169–207.
28 M. Sandoval-Paz, M. Sotelo-Lerma, A. Mendoza-Galvan and R. Ramírez-Bon, *Thin Solid Films*, 2007, **515**, 3356–3362.
29 Y.-P. Zhu, J. Li, T.-Y. Ma, Y.-P. Liu, G. Du and Z.-Y. Yuan, *J. Mater. Chem. A*, 2014, **2**, 1093–1101.
30 K. S. Suslick and G. J. Price, *Annu. Rev. Mater. Sci.*, 1999, **29**, 295–326.
31 Ö. Andaç, Ş. Murat Telli, M. Tatlier and A. Erdem-Şenatalar, *Microporous Mesoporous Mater.*, 2006, **88**, 72–76.
32 X. K. Wang, G. H. Chen and W. L. Guo, *Molecules*, 2003, **8**, 40–44.
33 S. M. K. Amir Hassanjani-Roshana, M. Reza Vaezi and A. Shokuhfar, *J. Ceram. Process. Res.*, 2011, **12**, 299–303.
34 H. Kim, C. Gilmore, A. Pique, J. Horwitz, H. Mattoussi, H. Murata, Z. Kafafi and D. Chrisey, *J. Appl. Phys.*, 1999, **86**, 6451–6461.
35 L. Fan, P. Wang, Z. Zheng, X. Zhu, Z. Zhang, Y. Zhang, P. Li and M. Yang, *Mater. Res. Bull.*, 2012, **47**, 3238–3242.
36 M. M. Adachi, A. J. Labelle, S. M. Thon, X. Lan, S. Hoogland and E. H. Sargent, *Sci. Rep.*, 2013, **3**, 2928–2933.
37 J.-Y. Chen, *Phys. E*, 2011, **44**, 43–48.
38 M. A. Hines and G. D. Scholes, *Adv. Mater.*, 2003, **15**, 1844–1849.
39 I. Moreels, K. Lambert, D. Smeets, D. De Muynck, T. Nollet, J. C. Martins, F. Vanhaecke, A. Vantomme, C. Delerue and G. Allan, *ACS Nano*, 2009, **3**, 3023–3030.
40 T. J. Macdonald, J. Xu, S. Elmas, Y. J. Mange, W. M. Skinner, H. Xu and T. Nann, *Nanomaterials*, 2014, **4**, 256–266.
41 J. He, H. Lindström, A. Hagfeldt and S.-E. Lindquist, *J. Phys. Chem. B*, 1999, **103**, 8940–8943.
42 S. Yang, X. Wen, W. Zhang and S. Yang, *J. Electrochem. Soc.*, 2005, **152**, G220–G226.
43 H. Zhou, Y. Tang, J. Zhai, S. Wang, Z. Tang and L. Jiang, *Sensors*, 2009, **9**, 1094–1107.
44 Y. Xu, J. Guo, T. Wei, X. Chen, Q. Yang and S. Yang, *Nanoscale*, 2013, **5**, 1993–2001.
45 C. J. M. Zhang, W. Dong, F. Zheng, L. Fang, X. Su and M. Shen, *Appl. Phys. Lett.*, 2013, **103**, 102902–102906.
46 T. Oekermann, T. Yoshida, D. Schlettwein, T. Sugiura and H. Minoura, *Phys. Chem. Chem. Phys.*, 2001, **3**, 3387–3392.
47 S.-H. Kao, Z.-L. Tseng, P.-Y. Ho, C.-Y. Kao, S. Thiyagu and C.-F. Lin, *J. Mater. Chem. A*, 2013, **1**, 14641–14648.